Bioactive Materials 17 (2022) 276–288

Contents lists available at ScienceDirect

Bioactive Materials

journal homepage: www.keaipublishing.com/en/journals/bioactive-materials

Oxygen-evolving photosynthetic cyanobacteria for 2D bismuthene radiosensitizer-enhanced cancer radiotherapy

Rong Chai [a], Luodan Yu [b], Caihong Dong [c], Yipengchen Yin [a], Sheng Wang [d,**], Yu Chen [b,*], Qin Zhang [a,***]

[a] Department of Radiation Oncology, Shanghai Chest Hospital, Shanghai Jiao Tong University, Shanghai, 200030, PR China
[b] Materdicine Lab, School of Life Sciences, Shanghai University, Shanghai, 200444, PR China
[c] Department of Ultrasound, Zhongshan Hospital, Fudan University, and Shanghai Institute of Medical Imaging, Shanghai, 200032, PR China
[d] Department of Colorectal Surgery, Fudan University Shanghai Cancer Center, Shanghai, 200032, PR China

ARTICLE INFO

Keywords:
Cyanobacteria
Photosynthesis
2D bismuthene
Radiosensitization
Hypoxia alleviation

ABSTRACT

The local hypoxic tumor environment substantially hampers the therapeutic efficiency of radiotherapy, which typically requires the large X-ray doses for tumor treatment but induces the serious side effects. Herein, a biomimetic radiosensitized platform based on a natural *in-situ* oxygen-evolving photosynthetic cyanobacteria combined with two-dimensional (2D) bismuthene with high atomic-number (Z) components, is designed and engineered to effectively modulate the radiotherapy-resistant hypoxic tumor environment and achieve sufficient radiation energy deposition into tumor. Upon the exogenous sequential irradiation of 660 nm laser and X-ray beam, continuous photosynthetic oxygen evolution by the cyanobacteria and considerable generation of reactive oxygen species by the 2D bismuthene radiosensitizer substantially augmented the therapeutic efficacy of radiotherapy and suppressed the *in vivo* tumor growth, as demonstrated on both LLC-lung tumor xenograft-bearing C57/B6 mice model and 4T1-breast tumor xenograft-bearing Balb/c mice model, further demonstrating the photosynthetic hypoxia-alleviation capability and radiosensitization performance of the engineered biomimetic radiosensitized platform. This work exemplifies a distinct paradigm on the construction of microorganism-enabled tumor-microenvironment modulation and nanoradiosensitizer-augmented radiotherapy for efficient tumor treatment.

1. Introduction

Radiation therapy (RT) is one of the crucial therapeutic modalities for cancer treatment [1], in which high-energy ionizing radiation (*e.g.*, X-ray, γ-ray) applied on the target tissues can either directly damage biomacromolecules or indirectly ionize the surrounding water to generate reactive oxygen species (ROS), and subsequently induce DNA damage and cell apoptosis [2–4]. In this process, oxygen in the microenvironment can anchor the broken ends of DNA, forming a stable organic peroxides group for hindering the further DNA repair. Hence, oxygen has been demonstrated to act as one of the most effective radiosensitizers [5]. However, the great majority of solid tumors will inevitably encounter hypoxic tumor microenvironment (TME) due to the rapid growth of tumor [6,7]. In addition, normal tissues under exposure to the radiation beam would also be non-selectively damaged, resulting in severe side effects during RT [8]. In order to protect the surrounding normal tissues, the application of RT doses are substantially limited [9], which however induces unsatisfied therapeutic outcome of RT and undesirable tumor relapse subsequently.

To enhance the therapeutic efficacy of RT, diverse strategies have been developed to address the hypoxia-associated RT resistance, *i.e.*, the use of MnO_2 nanoparticles for *in-situ* catalytic oxygen production and the physical oxygen delivery system by perfluorocarbon compounds [10–12]. These localized oxygenation platforms have been revealed to alleviate the hypoxia of TME and enhance the RT outcomes. However, these approaches still suffer several technically unsolved critical issues

Peer review under responsibility of KeAi Communications Co., Ltd.
* Corresponding author.
** Corresponding author.
*** Corresponding author.
E-mail addresses: wangs601@163.com (S. Wang), chenyuedu@shu.edu.cn (Y. Chen), zhangqin@shsmu.edu.cn (Q. Zhang).

https://doi.org/10.1016/j.bioactmat.2022.01.014
Received 27 October 2021; Received in revised form 3 January 2022; Accepted 10 January 2022
Available online 20 January 2022

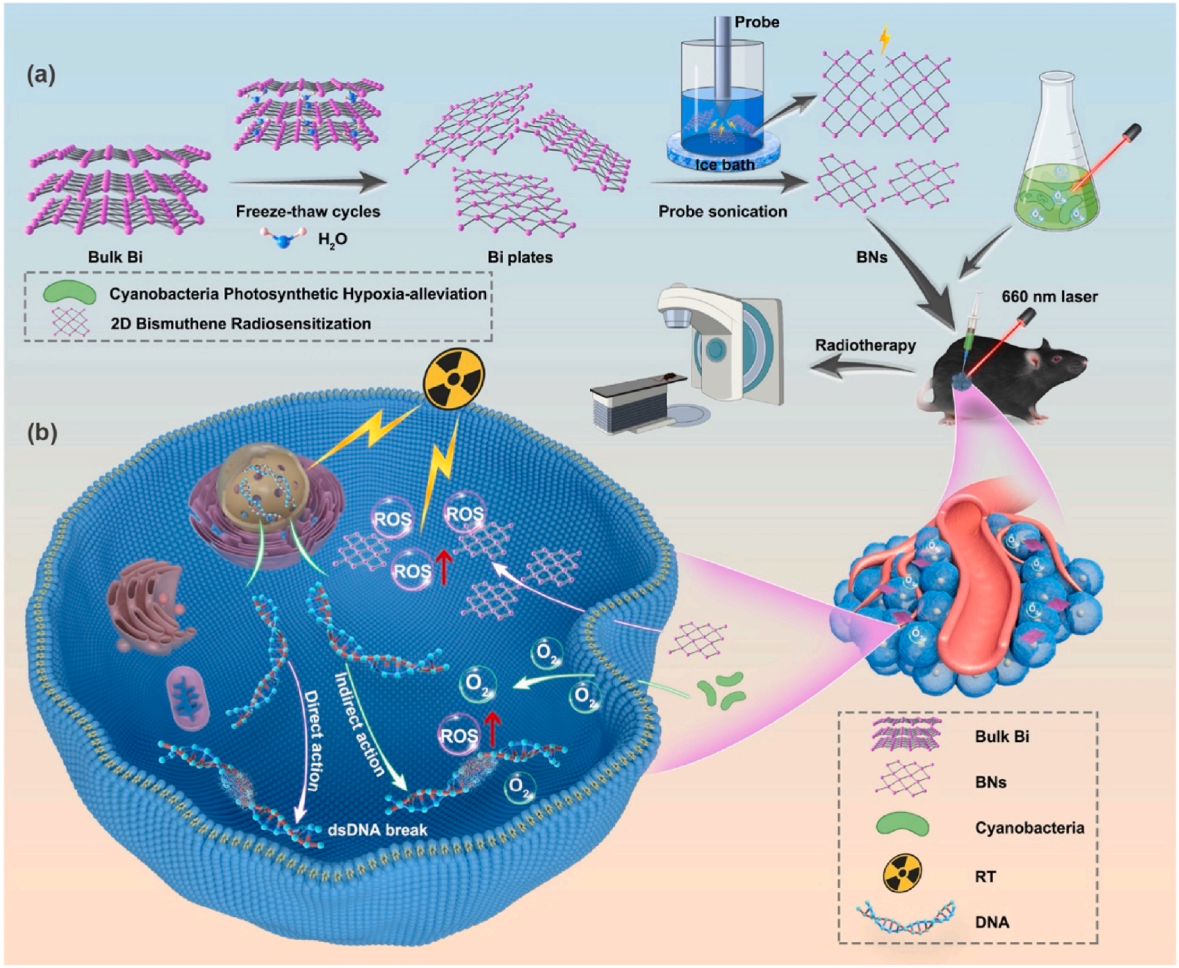

Fig. 1. (a) Schematic illustration of the synthesis of 2D bismuthene nanosheet *via* a facile top-down method: water mediated freeze-thaw cycles and probe sonication procession, during which the 2D structural nanosheet is exfoliated from bulk material effectively. **(b)** The scheme of tumor radiotherapy of the engineered biomimetic radiosensitized platform by integrating cyanobacterial and 2D BNs for photosynthetic hypoxia-alleviation and overproduction of ROS to doubly enhance the RT efficiency.

that prevent their further clinical translation and applications, such as undesirable biocompatibility and insufficient hypoxia-improving efficiency, where most of the administered oxygenation nanoplatforms would be captured by the mononuclear phagocyte system and the high uptake in major organs increases the risk of systemic toxicity [13,14]. Alternatively, microalgae, as a photoautotrophic natural resource, has been recently employed as a distinct oxygen-evolving agent for wound healing and hypoxia-associated tumor therapy [13,15,16]. Especially, microalgae has been extensively utilized in food, biofuel, health products and environmental pollution control field [17]. Recent progress of microalgae application has been focused on the biomedical field such as bioanalysis [18,19], tissue engineering [20], wound healing [21], drug delivery [22] and tumor therapy [23,24], which has also been demonstrated to feature high biocompatibility and low toxicity both *in vitro* and *in vivo*. Cyanobacteria range from unicellular to filamentous and include colonial species, which are capable of converting sun light energy to chemical energy with the release of oxygen, playing a key role in the transition of the early oxygen-poor atmosphere into an oxidizing one [25]. Phototrophic eukaryotes perform photosynthesis in plastids that are thought to evolved from cyanobacteria *via* endosymbiosis. With subsequent genetic integration, these endosymbiotic cyanobacteria then evolve into specialized organelles such as chloroplasts [25]. The chlorophyll on the thylakoid membrane works indispensably during the photosynthesis process. It is herein anticipated that this low-cost, safe and naturally abundant photon-powered cyanobacteria can be potentially developed as the hypoxia-alleviating agent by *in-situ* photosynthetic oxygen generation to improve the RT efficacy against tumor.

Radiosensitizers can selectively enhance the radiation-killing effect of tumor cells without risking the surrounding normal cells by overproducing ROS and further accelerating double-stranded DNA damage, which is generally regarded as an effective strategy to improve the radiation-therapeutic outcome with a relatively low dose of X-ray, reducing undesirable radiation energy deposition [9,26,27]. The nanoagents with high atomic-number (Z) bucomponents as introduced into the tumor region is considered as an effective approach to enlarge the contrast between normal and tumor tissue [28–31]. These nanosystems feature large X-ray attenuation coefficients, absorb X-rays to release photoelectrons, Auger electrons and Compton electrons for interacting with biomacromolecules and H_2O to generate ROS, and enhance the RT effects subsequently. However, the practical application of high-Z radiosensitizers is impeded due to the low biocompatibility and complex synthesis process, which further cause undefined biosafety issues *in vivo* [32]. 2D nanomaterials such as graphene, black phosphorus and MXenes have spiked substantial research interest in biomedical field due to their noticeable physiochemical property and biological effect [33–35]. More recently, the distinct 2D ultrathin bismuthene nanosheets (BNs) have potentiated the multipurpose biomedical uses [36]. Due to their unique optical performance, high biocompatibility and facile synthetic process, BNs have exerted the specific function in disease

theranostics such as photoacoustic/computed tomography (PA/CT) imaging and photothermal therapy (PTT) [37]. Especially, 2D bismuthene possesses the high-Z element of bismuth, therefore these 2D BNs are herein theoretically considered as the alternative but efficient radiosensitizer for augmenting the RT efficiency.

In this work, we rationally integrate photosynthetic cyanobacterial cells (*Synechococcus elongatus* PCC 7942 strain) for photosynthetic oxygenation and subsequent tumor-hypoxia alleviation with 2D ultrathin BNs as radiosensitizer for dual enhancement of the RT efficiency on tumor treatment (Fig. 1). Upon the irradiation of 660 nm laser, the increased O_2 generation by cyanobacterial photosynthesis could effectively alleviate the tumor-hypoxic condition both *in vitro* and *in vivo*. Meanwhile, the overproduced ROS in response to X-ray irradiation on 2D bismuthene then vigorously breaks DNA strands, which are further sufficiently anchored by the freshly generated oxygen in TME. This process induces considerable DNA breakage for efficient tumor destruction. The present design validates the biomimetic modulation of tumor-hypoxic microenvironment (photosynthetic oxygenation by cyanobacterial cells) and integrates an emerging radiosensitizer (2D bismuthene) for the production of large-amount ROS, which finally doubles and synergizes the therapeutic efficiency of RT against tumor.

2. Material and methods

2.1. Chemicals

BG11 medium was purchased from Freshwater Algae Culture Collection at the Institute of Hydrobiology (Wuhan, Hubei, China). Bismuth (powder, 325 mesh, 99.5%) was purchased from Alfa-Aesar Co., Ltd (Shanghai, China). Roswell Park Memorial Institute (RPMI) 1640 medium, High glucose DMEM medium, fetal bovine serum (FBS), phosphate buffer saline (PBS), penicillin-streptomycin and trypsin enzyme were purchased from Thermo Fisher Scientific (Waltham, MA, USA). $[Ru(dpp)_3]Cl_2$ was obtained from Alfa-Aesar Co. Ltd (Shanghai, China). Cell Counting Kit-8 (CCK-8) was bought from Dojindo Laboratories (Tokyo, Japan). Crystal Violet Staining Solution and 2′,7′-dichlorofluorescin diacetate (DCFH-DA) was purchased from Beyotime (Shanghai, China). 4% Paraformaldehyde, DAPI stain solution and bovine serum albumin (BSA) were purchased from Sangon Biotech (Shanghai, China). Triton X-100 was obtained from Diamond (Shanghai, China). γ-H2AX antibody were purchased from Cell Signaling technology (Danvers, MA, USA). 2.5% glutaraldehyde fixative was obtained from Servicebio (Wuhan, Hubei, China). Anti-hypoxia-inducible factor 1alpha (HIF-1α) antibody was purchased from Santa Cruz Biotechnology (Dallas, Texas, USA). Annexin V-FITC/PI apoptosis kit was obtained from Multi Sciences (Hangzhou, Zhejiang, China). All chemical reagents were used directly without further depuration.

2.2. Culture of the cyanobacteria

Cyanobacteria *Synechococcus elongatus* PCC 7942 strain was obtained from Freshwater Algae Culture Collection at the Institute of Hydrobiology (FACHB), Chinese Academy of Sciences (CAS). It was cultured in an Erlenmeyer flask using nitrogen-containing BG11 medium. With the light irradiation of a 12 h shift, the cyanobacterial cells were continuously vibrated in a constant temperature shaker (with the sizes of 50 cm × 63 cm × 45 cm) at 25 °C, 140 rpm, outfitted with a compact fluorescent lamp (rated at 10 W, 4000 K). The photosynthetic photon flux density (PPFD) was 337 μmol m^{-2} s^{-1}.

2.3. Preparation of 2D bismuthene nanosheets

The 2D bismuthene nanosheets were prepared *via* a top-down method. Two steps were adopted to exfoliate the layered bulk Bi to prepare 2D bismuthene structure: freeze-thaw cycles mediated by water molecule accompanied with probe ultra-sonication at a relatively low energy (200 W, 1 h). First, 1.0 g bismuth powder was dissolved in 60 mL ultra-pure water. With continuous and vigorous stirring for 1 h, the obtained mixture solution was frozen in the refrigerator at −80 °C for 4 h. Then, the frozen mixture was placed in ultrasonic bath to thaw into liquid state. Finally, the melting mixture was sonicated for 1 h at 200 W persistently. This procedure was repeated for ten times.

2.4. Characterization of cyanobacterial cells and 2D bismuthene

The cyanobacterial cells were characterized by bio-transmission electron microscopy (bio-TEM) with negative staining technique (HITACHI H-7650, Japan). Characterization of 2D bismuthene were performed by transmission electron microscopy (TEM), scanning transmission electron microscopy (STEM), corresponding energy dispersive X-ray spectroscopy (EDS) and element mapping, selective area electron diffraction (SAED) pattern analysis (JEM-F200, Japan). Zeta potential and dynamic light scattering (DLS) distribution was analyzed by a Zeta sizer Nanoseries (Zetasizer NANO ZSE, UK). The relatively quantitative elemental analysis was performed by inductively coupled plasma-atomic emission spectrometry (ICP-AES, Optima 7300 DV, US).

2.5. Photosynthetic oxygen-evolving assay of cyanobacterial suspension

To investigate the photosynthetic oxygen-evolving capacity, a portable dissolved oxygen electrode was used to detect the dissolved oxygen (DO) in cyanobacterial suspension. Before detection, the suspension of cyanobacteria (10 mL in beaker) was sealed in dark environment for 30 min to exhaust the remaining oxygen. Then the suspensions of different concentrations (0, 1.25, 2.5, 5×10^7 cell mL^{-1}) were irradiated under 660 nm laser for 20 min and the DO were recorded simultaneously. To investigate the influence of power density on photosynthesis, the different irradiation power densities (0, 10, 20, and 30 mW cm^{-2}) were then applied. After the treatment, the ascent of DO level were recorded.

2.6. In vitro cellular oxygen-evolving assay

The oxygen production capacity was detected by confocal laser scanning microscope using a hypoxia probe $[Ru(dpp)_3]Cl_2$. Initially, LLC cells were seeded into the confocal disk at a cell density of 10^5 cells/disk. Then, the attached cells were cultured in hypoxic condition ($pO_2 = 1\%$) for 12 h. The cyanobacteria group were then incubated with cyanobacteria ([cyanobacteria] $= 1 \times 10^7$ cells mL^{-1}) with or without laser irradiation (660 nm, 20 mW cm^{-2}, 15 min). The laser group were irradiated by 660 nm laser for 15 min under the same condition. After different treatment process, cells were then incubated with hypoxia probe $[Ru(dpp)_3]Cl_2$ (10 μg mL^{-1}) for another 3 h. The cells were finally washed by PBS for three times and then observed under confocal microscope (Ex: 488 nm, Em: 610 nm).

For HIF-1α expression in hypoxia or normoxic cells, LLC cancer cells were seeded into six-well plates with a density of 1×10^5 cells per well. After attachment, LLC cells were placed in a hypoxic condition (1% O_2) or a normoxic condition for 12 h, respectively. Subsequently, the medium was removed completely and replaced by 1 mL of fresh DMEM containing cyanobacteria (1×10^7 cells mL^{-1}) with or without laser irradiation (20 mW cm^{-2}, 15 min). After 12 h, the cells were collected and analyzed by western blotting analysis.

2.7. In vitro cellular uptake of BNs

Initially, LLC cells were seeded into the confocal disk at a cell density of 10^5 cells/disk. After attachment, the LLC cells were incubated with Rhodamine-B-labeled BNs for 1 h and 2 h. Then, the Rhodamine-B-labeled BNs were rinsed by PBS and cell nucleus were dyed with DAPI before observed under confocal microscope.

2.8. In vitro photothermal effect evaluation

LLC cancer cells were seeded into six-well plates with a density of 1 × 10^5 cells per well. After attachment, the BNs and cyanobacteria were added into the well ([BNs] = 200 μg mL^{-1}, [cyanobacteria] = 1 × 10^7 cells mL^{-1}). Then the cells were irradiated by 660 nm laser (20 mW cm^{-2}, 15 min). The thermal images and corresponding temperature changes were recorded by a photothermal camera.

2.9. In vitro biocompatibility and cell viability profile after varied treatments

LLC tumor cells were incubated in the 96-well plate at a density of 8 × 10^3 cells $well^{-1}$ for 12 h to attach. Then, the cyanobacteria (up to 1.4 × 10^7 cells mL^{-1}) and BNs (maximum of 200 μg mL^{-1}) of different concentrations were supplemented for another 24 h to assay biocompatibility profile. The treatment group were applied to RT (4 Gy), RT + Cyan (with laser irradiation, 660 nm, 20 mW cm^{-2}, 15 min), RT + BNs ([BNs] = 200 μg mL^{-1}), RT + Cyan + BNs (1 × 10^7 cells mL^{-1}). At different time points after RT (12, 24, 48, and 72 h), the previous medium was replaced into fresh ones containing 10% CCK8 reagent for 2 h incubation in the dark. Absorbance at 450 nm was measured by microplate spectrophotometer (Biotek Eon, America).

2.10. In vitro clonogenic assay

LLC cells were seeded in 6-well plates incubated for 24 h to attach, then the hypoxic groups were further incubated in the hypoxic incubator for another 3 h before RT. The treatment groups were then incubated with BNs + Cyan ([cyanobacteria] = 1 × 10^7 cells mL^{-1}, [BNs] = 20 μg mL^{-1}) for 2 h and then irradiated with X-ray (0, 2, 4 and 6 Gy). The cells were incubated for 10 days, fixed with an-hydrous ethanol and stained with Crystal violet. The surviving fraction (SF) was determined by the final colonies.

2.11. In vitro apoptosis analysis by flow cytometry

LLC cells were seeded in 6-well plates and incubated for 24 h to attach. Then, the cyanobacteria (1 × 10^7 cells mL^{-1}) and BNs (200 μg mL^{-1}) were supplemented and the cyanobacteria contained groups were irradiated by 660 nm laser before RT (4Gy). After 48 h, the cells were collected and analyzed by flow cytometry.

2.12. In vitro ROS detection

The *in vitro* cellular hydroxyl radical generation detection was tested by the cellular DCFH-DA assay. LLC tumor cells were initially inoculated into the 12-well plates at a density of 10^4 per well. Cell were allowed to attach for 12 h and then further incubated in normoxic or hypoxic condition for another 12 h, respectively. The supplementations of cyanobacteria and BNs ([cyanobacteria] = 1 × 10^7 cells mL^{-1}, [BNs] = 20 μg mL^{-1}) containing full medium, and the DCFH-DA probe and DAPI were directly added before 4 Gy RT. Immediately after RT treatment, the cells were observed under a confocal laser scanning microscope (CLSM, ZEISS LSM710, Germany).

2.13. In vitro dsDNA fracture detection

For γ-H2AX immunofluorescence analysis, LLC cells were seeded in 12-well plates at a density of 10^4 per well. Cell were allowed to attach for 12 h and the further incubated in normoxic or hypoxic condition for another 12 h, respectively. The cells were incubated with cyanobacteria and BNs ([cyanobacteria] = 1 × 10^7 cells mL^{-1}, [BNs] = 20 μg mL^{-1}) and then irradiated with X-ray (4 Gy). Then, the cells were fixed by 4% paraformaldehyde for 10 min, incubated with 0.2% Triton X-100 for 10 min, incubated with 1% BSA for 1 h and incubated with the primary antibody (rabbit monoclonal *anti*-phospho-histone γ-H2AX, 1% BSA in PBS, 1:500) overnight at 4 °C. The cells were finally incubated with the secondary antibody (anti-rabbit Dylight 594, 1% BSA in PBS, 1: 500) for 1 h, stained with DAPI (1 μg mL^{-1}) for 5 min and observed with CLSM (ZEISS LSM710, Germany).

2.14. In vivo oxygen-evolving photoacoustic (PA) imaging

The oxygen-evolving of cyanobacteria intratumorally were evaluated by VEVO LAZR-X photoacoustic imaging station of "Oxyhemo" mode. The PA/US image were recorded at different time points (before/after cyanobacteria injection, after 660 nm laser irradiation). Then, the average oxygen saturation of tumor tissue was calculated by the VEVO LAZR-X system software package. ([cyanobacteria] = 1 × 10^8 cells mL^{-1}, 660 nm, 50 mW cm^{-2}, 10 min).

2.15. In vivo biocompatibility assessment

Healthy 8-week-old Institute of Cancer Research (ICR) mouse were randomly divided into three groups (n = 3) and then injected with PBS and BNs + Cyan ([cyanobacteria] = 5 × 10^8 cells mL^{-1}), [BNs] = 50 mg kg^{-1}) intravenously for 3 and 30 days respectively. The body weights of chronic toxicity assay group were recorded every three days. At the endpoint of each group, serum of these mice were collected for blood biochemistry analysis. The prime organs (heart, liver, spleen, lung and kidneys) were dissected and evaluated the acute or chronic toxicity by hematoxylin and eosin (H&E) staining analysis.

2.16. In vivo fluorescence imaging of mice

The 6-week-old female C57/B6 mice bearing orthotopic LLC cells tumors (n = 3) were administered with intratumoral injection of freshly prepared cyanobacteria (5 × 10^7 cells mL^{-1}, 20 μL per mouse). Another three 6-week-old female C57/B6 mice were administered with a intravenous injection (1 × 10^7 cells mL^{-1}, 100 μL per mouse). In addition, the urine and feces of different timepoints were also collected for fluorescence imaging. The retention time and elimination of cyanobacteria were detected by fluorescence imaging with an excitation wavelength of 640 nm and emission wavelength of 694 nm (IVIS® spectrum, PerkinElmer, USA).

2.17. In vivo tumor radiotherapy on the LLC-tumor xenograft-bearing C57/B6 mice model

First, twenty-five female 6-week C57/B6 mice were randomly divided into five groups (n = 5): (1) control, (2) RT (8 Gy), (3) RT (8 Gy) + Cyan (660 nm, 50 mW cm^{-2}, 10 min), (4) RT (8 Gy) + BNs, (5) RT (8 Gy) + BNs + Cyan (660 nm, 50 mW cm^{-2}, 10 min). 3 × 10^6 cells were subcutaneous injected on the right groin. When the tumor volume reached around 150 mm^3, the different treatment was carried out. For respective treatment groups, mice were intratumorally treated with cyanobacteria and BNs. There were 30 min interval between 660 nm laser irradiation and RT. Then the tumor-bearing mice were taken good care for their revival. During the monitoring period, the mice were weighted every other day, while the tumor size profiles of mice in each group were measured with digital caliper perpendicularly (l_1, l_2, $l_1 > l_2$). Tumor volume were calculated according to the following equation:

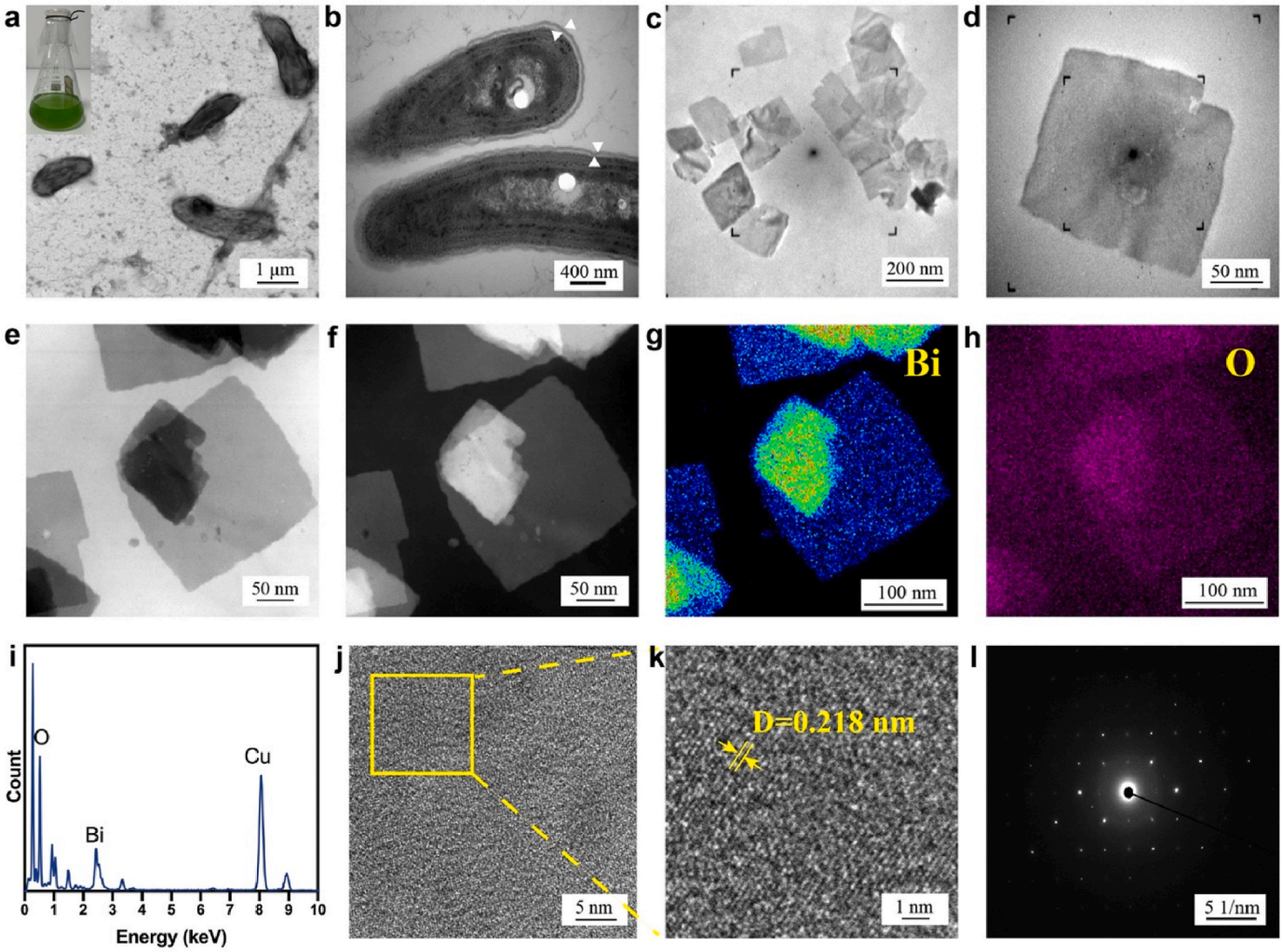

Fig. 2. Detailed characterizations of 2D bismuthene and cyanobacterial cells. (a) Bio-TEM image of cyanobacterial cells with negative staining. Inset, green culture of cyanobacterial cells. **(b)** TEM image of cyanobacterial cells at high magnification. TEM images of 2D bismuthene at **(c)** low and **(d)** high magnifications. **(e)** Bright-field and **(f)** dark-field STEM images of 2D bismuthene. **(g, h)** EDS mapping images of 2D bismuthene (g: Bi, h: O). **(i)** EDS spectrum of 2D bismuthene. **(j)** HAADF-STEM image and **(k)** enlarged image of 2D bismuthene. **(l)** SAED pattern of 2D bismuthene.

$$V = \frac{1}{2} l_1 \times {l_2}^2$$

After the follow-up, the mice were then anesthetized by intraperitoneal injection of 80 mg kg^{-1} pentobarbital sodium. The tumors were collected for further H&E, TUNEL and antigen Ki-67 staining. The prime organs of these mice (heart, liver, spleen, lung and kidneys) were also collected to value the safety of treatment.

2.18. In vivo tumor radiotherapy on the 4T1-tumor xenograft-bearing Balb/c mice model

Twenty 6-week female Balb/c mice bearing 150 mm^3 4T1 tumors were stochastically allocated into five groups (n = 4): (1) control, (2) RT, (3) RT + Cyan (with 660 nm laser irradiation), (4) RT + BNs, (5) RT + BNs + Cyan (with 660 nm laser irradiation). The interval between 660 nm laser irradiation (50 mW cm^{-2}, 10 min) and RT (6 Gy) were 30 min. Tumor size and body weight of the mice were recorded every other day. After the evaluation process for 14 days, mice were sacrificed by intraperitoneal injection of 80 mg kg^{-1} pentobarbital sodium. Tumor and major organs of each mouse were collected and H&E, TUNEL and antigen Ki-67 staining were implemented for pathological analysis. All the *in vivo* animal experiments were performed under the guidelines of Laboratory Animal Ethics Committee of Shanghai Chest Hospital (Shanghai, China; KS (Y)1623). All applicable international, national, and/or institutional guidelines for the care and use of animals were strictly followed.

2.19. Statistical analysis

Statistical analysis was conducted through Graphpad Prism 8.00. n.s. represented not significance; *P < 0.05 represented statistical significance; **P < 0.01 represented moderate statistical significance and ***P < 0.001 represented highly statistical significance.

3. Results and discussion

3.1. Detailed morphology, structure and composition characterization of cyanobacteria and 2D bismuthene

Cyanobacteria (*Synechococcus elongatus* PCC7942 strain) was cultured in BG11 medium and fresh medium was continuously supplied into the flask to make sure the microalgae cells healthily cultured in their mid-exponential phrase (OD_{730} = 0.4–0.7), forming a characteristic green color of the culture medium (Fig. 2a, inset). Photosynthetic

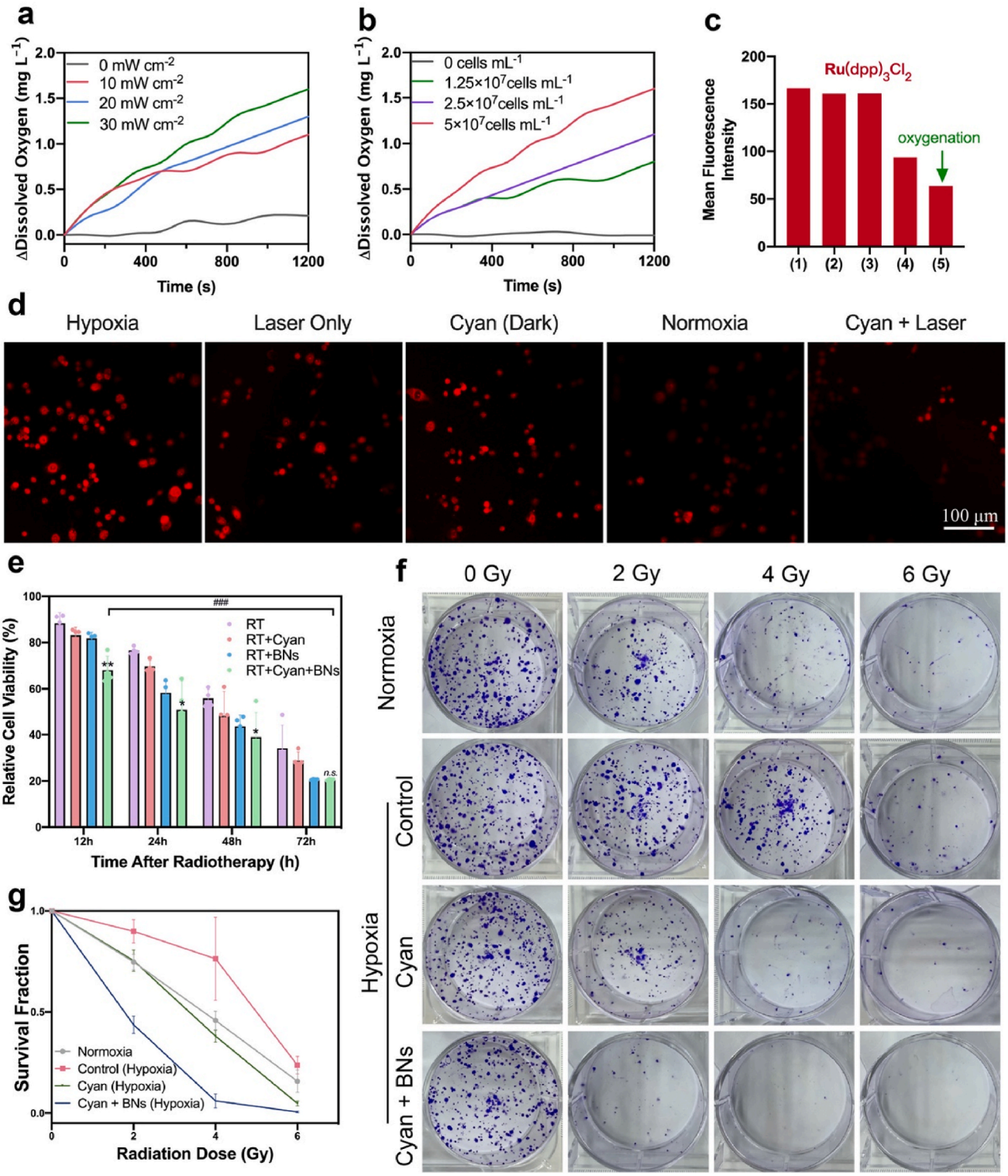

Fig. 3. *In vitro* photosynthetic oxygen evolution and cellular therapeutics. Dissolved oxygen level variations of the solution under 660 nm laser irradiation at **(a)** different irradiation power densities (0, 10, 20, and 30 mW cm^{-2}) and **(b)** different cyanobacterial concentrations (0, 1.25, 2.5, and 5 × 10^7 cell mL^{-1}). **(c)** The quantized fluorescence intensity of $[Ru(dpp)_3]Cl_2$-stained cells in each group. (1) Hypoxia group, (2) Laser Only group, (3) Cyan (Dark) group, (4) Normoxia group, (5) Cyan + Laser group. **(d)** Confocal fluorescence images of LLC tumor cells stained with $[Ru(dpp)_3]Cl_2$, showing intracellular O_2 level treated with cyanobacteria ([cyanobacteria] = 1 × 10^7 cells mL^{-1}) with or without laser irradiation (660 nm, 20 mW cm^{-2}, 15 min). Scale bars, 100 μm. **(e)** *In vitro* cell viability profile of LLC tumor cells after treatment of RT, RT + Cyan (with laser irradiation, 660 nm, 20 mW cm^{-2}, 15 min), RT + BNs ([BNs] = 200 μg mL^{-1}), RT + Cyan + BNs (660 nm, 20 mW cm^{-2}, 15 min [BNs] = 200 μg mL^{-1}) with the course of time after 4 Gy RT (12, 24, 48, and 72 h). **(f)** Clonogenic assay of LLC cells *in vitro*, revealing the augmented sensitivity of RT after cyanobacteria and BNs treatment (660 nm, 20 mW cm^{-2}, 15 min [BNs] = 200 μg mL^{-1}). **(g)** Survival fraction of clonogenic assay with the course of different radiation doses (2, 4, and 6 Gy). Data are presented as mean ± SD. n = 3 for each group. *n.s.* for non-significance compared to the RT group. *P < 0.05, **P < 0.01, ***P < 0.001 compared to the RT group.

machinery was embedded in the thylakoid membranes, which was organized into multiple concentric shells, forming a highly connected network. The detailed morphological features of cyanobacteria were characterized by bio-transmission electron microscopy (bio-TEM) and negative-staining technology. The cyanobacteria feature a rod shape with the average size of 0.4–1.0 μm in width and 2.0–4.0 μm in length. The bilayer membrane on the surface is clearly distinguished in TEM image (Fig. 2b). In the cross-sectional scheme, the cytoplasm contains multiple concentric ring-like membrane layers, called thylakoids, where the photosynthetic pigments and electron transport chains are located (Fig. S1, Supporting Information).

The 2D bismuthene nanosheets, a layered Bi-based Xene, were prepared by a typical exfoliation strategy [37]. It was synthesized *via* an ultrafacile freeze-thaw cycles mediated by water molecule and accompanied with sonication process to yield the layered structure. The probe ultra-sonication with a relatively low energy input plays an essential role in decreasing Bi-based flake size and exerting the stripping function, which is the prerequisite for the subsequent biomedical uses. As revealed by the TEM observation, after ten cycles of freeze-thaw and sonication process, the bulk Bi crystal was stripped into square layered nanosheets with the average sheet size of 200 nm (Fig. 2c–d). The particle-size distribution was also confirmed by dynamic light scattering (DLS) in aqueous solutions, which revealed that the average hydrodynamic diameter of the obtained 2D bismuthene nanosheets was around 356 nm and the Zeta potential was determined to be −1.57 mV (Fig. S2). The bright-field and dark-field scanning transmission electron microscopy (STEM) images combined with the corresponding energy dispersive X-ray spectroscopy (EDS) and element mapping (Fig. 2e–i) both proved the homogeneous distributions of Bi and O elements on the nanosheets surface. The O elements on the surface were introduced during the BNs stripping cycles because of the partial and mild oxidation, whereas the Bi component served as a high-Z element radiosensitizer. The atomic-resolution STEM image in high-angle annular dark-field (HAADF) mode revealed that the lattice spacing was 0.218 nm (Fig. 2j–k), which was consistent with the selective area electron diffraction (SAED) pattern (Fig. 2l). We further evaluated the stability of BNs at different pHs (Fig. S3). The nanosheets of BNs captured by TEM showed the stable 2D structure at pHs of 6.5 and 5.0. In addition, there were no obvious changes in absorbance of BNs solutions ([BNs] = 200 μg mL^{-1}) at 450 nm within 7 days, indicating that BNs would not aggregate or precipitate and was stable under these pH conditions.

3.2. Photosynthetic oxygen-evolving capability of cyanobacteria

Cyanobacteria-enabled robust oxygen production through photosynthesis plays an important role in alleviating hypoxic TME and subsequently reversing the radiotherapy resistance. Upon exposure to the red light (660 nm laser) irradiation, the oxygen production by cyanobacteria *in vitro* was assessed. A portable dissolved oxygen electrode was used to detect the dissolved oxygen (DO) in cyanobacterial suspension. Before detection, the suspension of cyanobacteria at a concentration of 5×10^7 cells mL^{-1} was sealed in the dark environment for 30 min to exhaust the remaining oxygen. The DO of the cyanobacterial suspension did not rise without light irradiation, indicating that the cyanobacteria could not perform photosynthetic oxygen generation in the dark environment. Upon the 660 nm laser irradiation, continuous and smooth oxygen generation was observed. The DO was observed with a maximum lift of 41 μmol L^{-1} in solution system under 20 mW cm^{-2} irradiation in 20 min (Fig. 3a). With the increase of irradiation power density (10, 20, and 30 mW cm^{-2}), the degree of photosynthetic oxygenation was enhanced. When cyanobacterial population reached 5×10^7 cells mL^{-1}, the DO elevation of 50 μmol L^{-1} could be achieved, demonstrating the vigorous photosynthetic oxygen-generating capacity of cyanobacteria in solution (Fig. 3b).

The capability of cellular photosynthetic oxygenation by cyanobacteria was explored using a intracellular hypoxia indicator $[Ru(dpp)_3]Cl_2$ [38]. In detail, Lewis tumor cells (LLC) were initially cultured in a hypoxia incubator with an O_2 partial pressure (pO_2) stabilized at 1% for 12 h to imitate the hypoxic environment of the tumor cells. Then, the hypoxic cells were incubated with cyanobacteria with/without laser (660 nm, 20 mW cm^{-2}, 15min) irradiation. The fluorescent intensity was detected by a confocal laser scanning microscope, which is inversely proportional to intracellular hypoxia condition. The scanning images and corresponding quantitative mean fluorescence intensity result of each group was illustrated (Fig. 3c–d). As expected, the red fluorescence of $[Ru(dpp)_3]Cl_2$ probe perished under co-incubation with cyanobacteria receiving laser irradiation, which was comparable with the intensity of normoxic condition ($pO_2 \approx 20\%$). The laser alone could not ameliorate the hypoxia condition. Especially, the incubation with cyanobacteria sealed-in-dark aggravated hypoxia due to the respiration of cyanobacteria in the dark.

In addition, hypoxia-inducible factor 1-α (HIF-1α), a subunit of a heterodimeric transcription factor HIF-1, is considered as the master transcriptional regulator of cellular and developmental response to hypoxia [39]. Under hypoxia condition, a notably high HIF-1α expression was observed. Intriguingly, the expression is markedly downregulated in the presence of cyanobacteria under light irradiation in hypoxic condition, in which the relative expression level of HIF-1α was 0.59 after quantifying (Fig. S4). The western blotting analysis reveals that cyanobacteria as a distinct oxygen-evolving platform could effectively alleviate intracellular hypoxia and downregulate HIF-1α expression.

3.3. Intracellular enhanced RT efficacy

Based on the distinct oxygen-evolving capability, the therapeutic effectiveness was further assessed *in vitro* using murine lung LLC tumor cell line. First, the cytocompatibility of cyanobacteria (up to 1.4×10^8 cells mL^{-1}) and BNs (concentration maximum of 200 μg mL^{-1}) was evaluated. The standard cell counting Kit-8 (CCK-8) assay results reveal that both cyanobacteria and BNs feature no obvious cytotoxicity after 24 h co-incubation (Fig. S5). The cellular uptake behavior of BNs by CLSM was also investigated (Fig. S6). According to the confocal microscopic images of LLC cells incubated with Rhodamine-B-labeled BNs (red), the cellular uptake of BNs was observed after co-incubation for 1 h and the uptake of BNs gradually increased over time. After 2 h incubation, the BNs were enriched in LLC cells. Furthermore, the *in vitro* treatment effectiveness was also explored *via* CCK-8 assay. Before receiving RT, the LLC tumor cells were respectively incubated with cyanobacteria at the population of 1×10^7 cells mL^{-1} upon laser irradiation for 15 min (660 nm, 20 mW cm^{-2}) and BNs at the concentration of 200 μg mL^{-1}. At the different time points after RT, the cell viability presented a downward trend (Fig. 3e). 11.7% of LLC cells which received RT only were dead at the time point of 12 h, while 65.9% counterparts were killed at 72 h. At the time of 48 h after RT, 61.0% of LLC tumor cells treated with Cyan + BNs were killed and 44.3% were killed by RT only, which demonstrated the effective RT sensitization of BNs and cyanobacteria. In order to clarify whether the continuous irradiation for 15 min caused elevated temperature and subsequent photothermal effects, the temperature-changing thermal images were

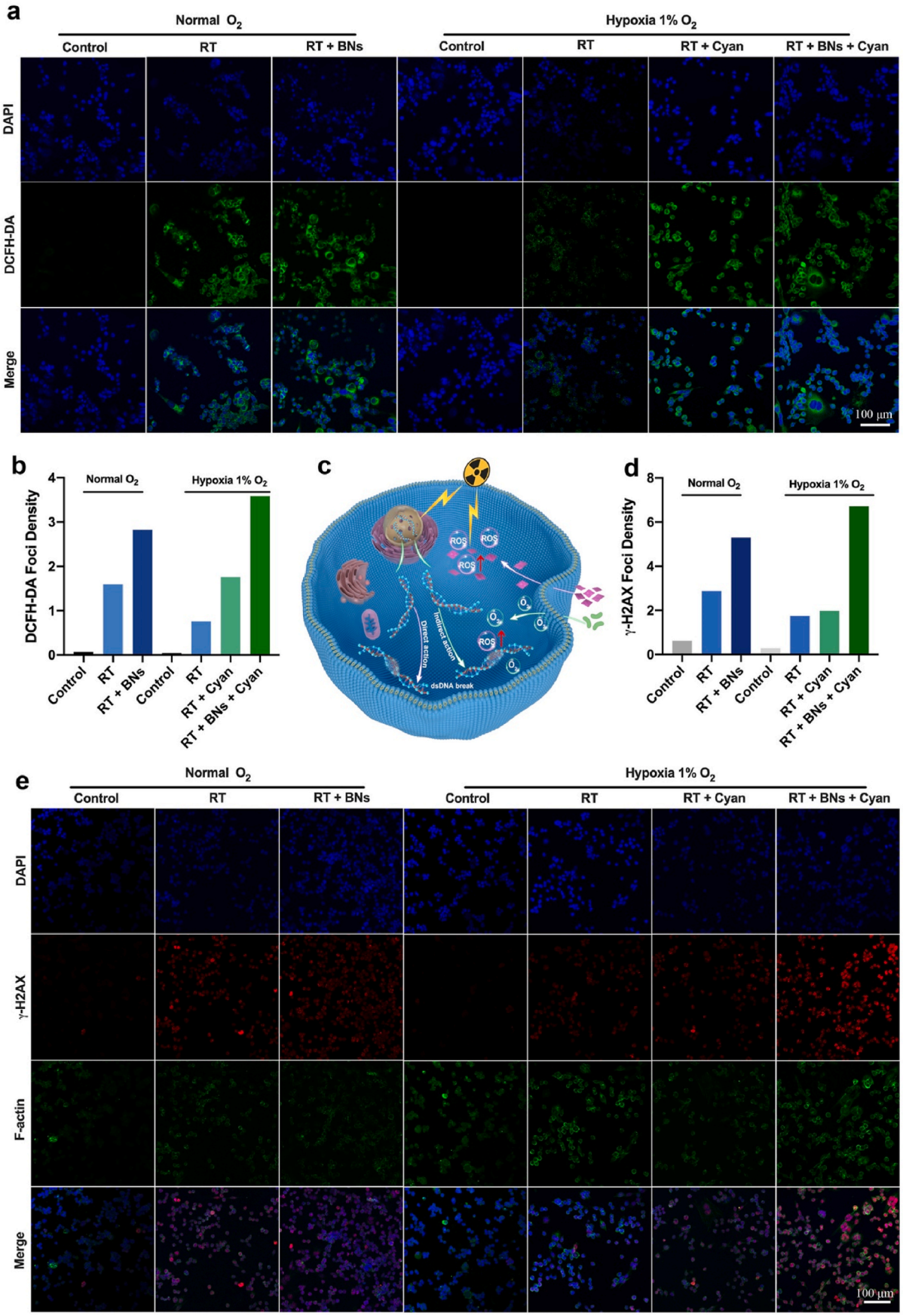

(caption on next page)

Fig. 4. *In vitro* ROS level and dsDNA damage assessment. (a) Confocal microscopy images of LLC tumor cells stained by DCFH-DA probe when treated with Cyan (660 nm, 20 mW cm^{-2}, 15 min), BNs and BNs + Cyan ([cyanobacteria] = 1 × 10^7 cells mL^{-1}, [BNs] = 200 μg mL^{-1}) in normoxic and hypoxic conditions. **(b)** Corresponding quantitative analysis of the DCFH-DA fluorescence density. **(c)** Scheme of the cellular ROS overproduction and dsDNA damage under the X-ray beam exposure. The overproduced ROS in response to X-ray irradiation on high-Z element-contained 2D BNs then vigorously breaks DNA strands, which are further sufficiently anchored by the freshly generated oxygen by cyanobacterial photosynthesis in TME. **(d, e)** Confocal microscopy images and corresponding quantitative analysis of LLC tumor cells stained by γ-H2AX bio-marker when treated with Cyan, BNs and BNs + Cyan (660 nm, 20 mW cm^{-2}, 15 min, [BNs] = 200 μg mL^{-1}) in normoxic and hypoxic conditions. Scale bars, 100 μm.

recorded (Fig. S7). Results indicated that both cyanobacteria and BNs showed no significant temperature elevation with laser irradiation (660 nm, 20 mW cm^{-2}, 15 min).

Encouraged by the CCK-8 results, we further evaluated the radiation-induced apoptosis by employing a typical clonogenic assay. We cultured the LLC cells in normoxic and hypoxic conditions, respectively. The hypoxic environment ($pO_2 = 1\%$) was herein used to imitate the hypoxic TME with RT resistance in clinical treatment. As expected, the surviving fraction (SF) of hypoxic cells was relatively higher than these cultured in normal oxygen pressure environment, exhibiting poor sensitivity to RT (Fig. 3f–g). When the cancer cells were treated with cyanobacteria and BNs (660 nm, 20 mW cm^{-2}, 15 min), the sparse cloning demonstrated the improved sensitivity of RT, and more cancer cells were killed and were proliferation-inhibited. Additionally, the apoptosis of LLC cells with the indicated treatment was also measured by flow cytometry (Fig. S8). Results elucidated that the maximum tumor killing rate of LLC cells was occurred in RT + Cyan + BNs group at 48 h after RT, which was in accordance with the results of CCK-8 viability assay.

We then used a green fluorescent ROS indicator, dichlorofluorescein diacetate (DCFH-DA), to assess the ROS production. Apart from directly damaging double-stranded DNA (dsDNA), radiation for killing the cancer cells depends more on indirect reaction with water in soft tissues to facilitate ROS generation, which then breaks dsDNA [40]. Confocal microscopy images of LLC tumor cells stained by DCFH-DA probe and corresponding quantitative fluorescence intensity results were depicted (Fig. 4a–b). Under normoxic condition, the fluorescence intensity of DCFH-DA from the BNs-treated LLC cells was much stronger than those in the cancer cells received RT only, indicating that BNs increased ROS production by enhancing energy dose deposition in tumor cells. In hypoxic group, the fluorescence intensity of RT group manifestly dropped comparing with the normoxic condition, which validated the radiation resistance of hypoxic tumor. After incubation with cyanobacteria and BNs, the increase in green fluorescence, about 4.7-times higher than RT only in hypoxic condition, indicated the double-radiosensitive profile of cyanobacteria and BNs. Consistent with CCK-8 assay, the strongest fluorescence intensity was observed in RT + BNs + Cyan group.

The overproduced ROS from BNs under X-ray irradiation then leads to considerable DNA breakage for efficient tumor destruction (Fig. 4c). Correspondingly, the degree of dsDNA fracture was disclosed using a bio-marker γ-H2AX, which formed immediately on the ends of broken DNA strands after radiation. Consistent with the ROS yield, the fluorescence intensity of BNs-treated group in normoxic condition increased sharply compared with RT group (Fig. 4d–e). Regardless of the decreased DNA breakage in hypoxic condition, the cyanobacterial photosynthetic oxygen-evolving and BNs radio-sensitization could improve the fluorescence intensity in a visible manner, further verifying the radiation-sensitizing capability of BNs and hypoxia-alleviating capability of cyanobacteria.

3.4. *In vivo oxygenation and tumor radiotherapy*

We then assessed the *in vivo* oxygen-evolving profile and tumor radiotherapy efficiency on LLC-tumor xenograft-bearing C57/B6 mice and 4T1-tumor xenograft-bearing Balb/c mice. Lung cancer and breast cancer are currently the most commonly diagnosed cancer and the leading cause of cancer death [41]. Prior to subsequent treatment, we systematically assured the biocompatibility of the cyanobacteria and BNs ([cyanobacteria] = 5 × 10^8 cells mL^{-1}), BNs ([BNs] = 50 mg kg^{-1}) on healthy Institute of Cancer Research (ICR) mouse. The treated mice were then sacrificed after 3 and 30 days, and their major organs and blood were collected to evaluate the acute or chronic toxicity, respectively. During the observation period, no obvious behavior changes and irregularity abnormalities of body weight were monitored compared with the control group. Blood biochemical results indicated no obvious inflammation response in both acute and long-term groups (Fig. S9). In addition, no obvious histological damage was monitored in the major organs (Fig. S10), indicating the reliable biosafety *in vivo*.

Notably, to further evaluate the retention time of cyanobacterial suspension *in vivo*, the fluorescence imaging of mice after intratumoral injection of cyanobacterial suspension during 7 days was recorded (Fig. S11). The results showed that the fluorescence intensity of tumor area attenuated in the subsequent time after injection. Compared with 0.5 h after injection, 15% radiant efficiency was observed at the 7th day, indicating that the cyanobacterial suspension was absorbed after injection and gradually eliminated by the body. In order to intelligibly observe the elimination profile of cyanobacteria in the body, we further evaluated the fluorescence imaging of mice after intravenous injection of cyanobacterial suspension and collected urine and feces for renal clearance and hepatic metabolism analysis at various time points (Fig. S12). The results signified that the clearance could be basically completed within 48 h after injection. After reaching the peak within 3 h, the fluorescence intensity then dropped rapidly and the excretion from renal and hepatic reached maximum at 6 h. Combined with excretion analysis performed by the fluorescence signals of urine and feces, the results indicated that the cyanobacteria could undergo both renal and hepatobiliary clearance routes after intravenous injection.

The *in vivo* oxygen-producing capability of cyanobacteria was then investigated according to a combined photoacoustic (PA) and ultrasound (US) imaging at oxygen hemoglobin model. Before administration of cyanobacteria, 4.1% of the average O_2 saturation (sO_2) percentage in tumor was recorded, validating the hypoxic condition of TME [42]. The PA signal exhibited no apparent changes once we completed the administration of cyanobacteria. After 660 nm laser irradiation for 10 min, the sO_2 presented a vigorous upward trend, revealing the desirable oxygen-producing capability and the successful penetration of light into mammalian tissue (Fig. 5b–c). According to the corresponding time-course quantitative analysis, the tumor sO_2 soared in the first 10 min post-injection. Peaking at approximately 21.5%, sO_2 displayed a decrease tendency. Even 1 h later, the sO_2 was still above the baseline, indicating the long-lasting oxygen-generating effect. Based on the above results, we chose the time point of 30 min post-injection for the follow-up RT intervention.

Based on the desirable biocompatibility and tumor oxygenation, we further evaluated the *in vivo* anti-tumor efficiency. The therapeutic experiment was carried out on the LLC-tumor xenograft-bearing C57/B6 mice when the tumor volume reached around 150 mm^3. The tumor-

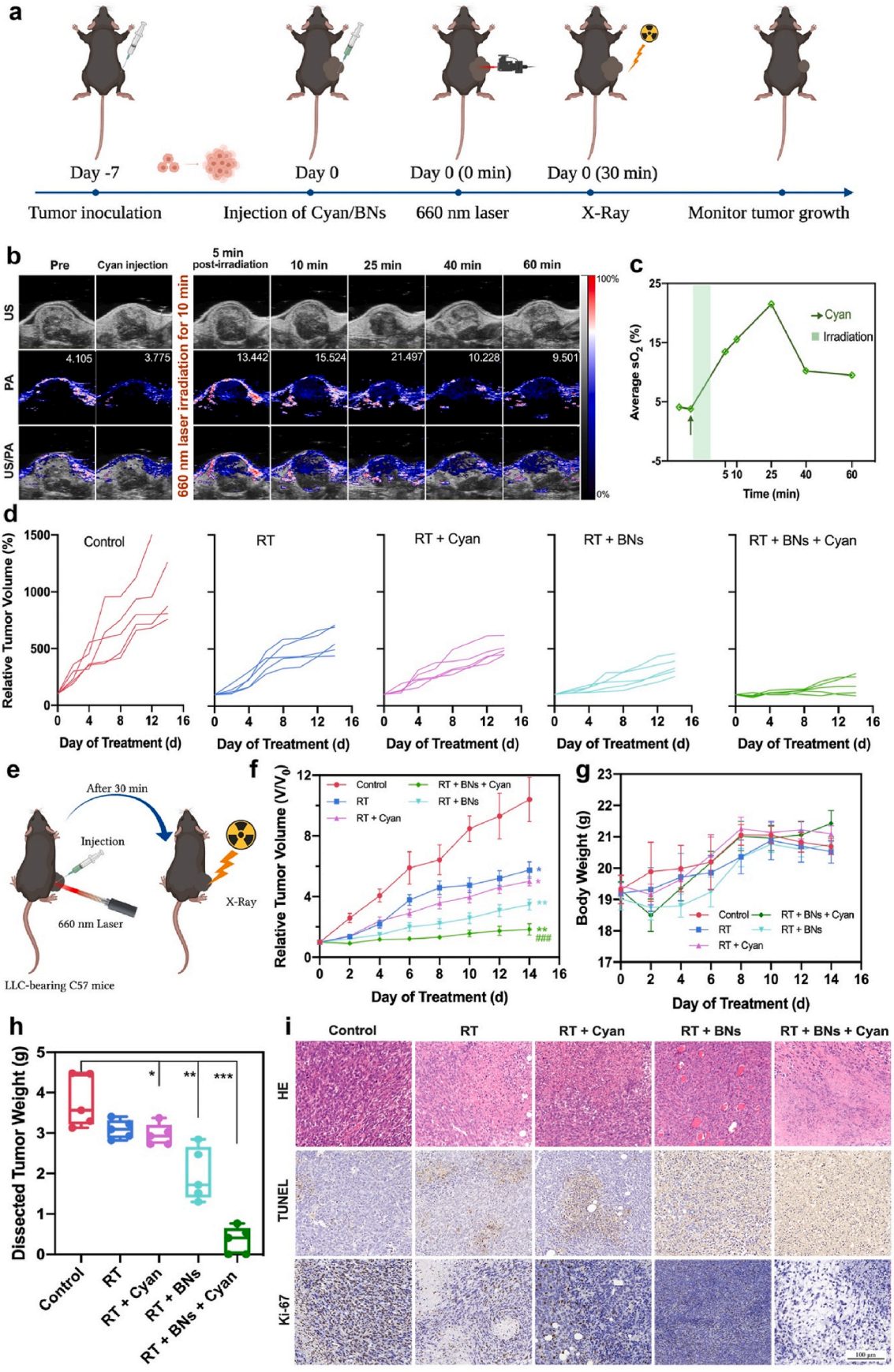

(caption on next page)

Fig. 5. *In vivo* oxygenation and enhanced tumor radiotherapy on the LLC-tumor xenograft-bearing C57/B6 mice model. (a) Schematic illustration of Cyan/BNs-enhanced tumor radiotherapy *in vivo* (Created with BioRender.com). **(b)** *In vivo* US and PA imaging, and their merged images of oxygen hemoglobin model in LLC tumor at different time points after administration of cyanobacteria ([cyanobacteria] = 1×10^8 cells mL^{-1}) and subsequent laser irradiation (660 nm, 50 mW cm^{-2}, 10 min) for *in vivo* tumor oxygenation assessment. **(c)** Corresponding quantitative analysis of time-course of O_2 saturation percentage according to the PA signals. The green-shadowed region indicates the laser irradiation time window. **(d)** Individual tumor-growth curves of mice after various treatments: group 1 for PBS, group 2 for RT, group 3 for RT + Cyan (with 660 nm laser irradiation), group 4 for RT + BNs and group 5 for RT + BNs + Cyan (with 660 nm laser irradiation). **(e)** Schematic illustration of specified cyanobacteria administration and following radiotherapy *in vivo*. **(f)** Tumor volumes and **(g)** body weights for each group of mice recorded every 2 days after various treatments (n = 5). **(h)** Average tumor weights for each group of dissected xenografts recorded after various treatments (n = 5). All data are presented as mean ± SD. *n.s.* for non-significance, *P < 0.05, **P < 0.01 compared to the control group. ###P < 0.001 compared to the RT group. **(i)** H&E, TUNEL, and antigen Ki-67 analysis of tumor slices subjected to various treatments.

bearing mice were divided randomly into 5 groups and accepted different therapeutic treatments (Fig. 5a), including control group, RT group, RT + Cyan group, RT + BNs group and combined RT + Cyan + BNs group. Mice that received cyanobacteria injection were then irradiated by 660 nm laser for 10 min for photosynthetic oxygen production. Thirty minutes afterwards, all the mice were received RT on the tumor site by using a squared-field X-ray irradiation. During the assessment period (14 days), the body weight and tumor size were carefully measured every other day to assess the therapeutic efficiency and healthy condition of mice. More significantly, the tumor-growth curve was depicted (Fig. 5d–f), and the results demonstrated that both weight and size of tumors were remarkably inhibited in the combined Cyan + BNs group compared with control group, which forcefully demonstrated the hypoxic TME-modulating capacity of cyanobacteria and the radiosensitive ability of 2D BNs *in vivo*. Averagely, the inhibitory rates of tumors in different groups were 91%, 74%, 57% and 49% in combined Cyan + BNs (with laser irradiation), BNs, Cyan and RT groups, respectively. The body-weight profiles of different treatment groups appeared no obvious difference as compared to the control group and remained at normal levels during the whole monitoring period, indicating the healthy status and no obvious side effect of the developed therapeutic modalities (Fig. 5g). At the end of treatments, we collected the tissues of tumor and major organs, which were measured *ex vivo* subsequently (Fig. 5h, Fig. S13). From the pathological features of the dissected major organs, the eligible *in vivo* treatment biosafety of cyanobacteria and BNs were demonstrated (Fig. S14). Hematoxylin and eosin (H&E)-stained ultrathin tumor sections showed the decreased tumor cell density and reduced proliferation (reflected by Ki-67 expression). The terminal deoxynucleotidyl transferase dUTP nick end labeling (TUNEL) staining showed the increased apoptosis level (Fig. 5i). In addition, the corresponding quantitative analysis of TUNEL and Ki-67 was also carried out (Fig. S16a). The combined RT + BNs + Cyan group showed the significantly increased TUNEL and decreased Ki-67 expression levels comparing with the control group. The pathological status was supportive of the outstanding antitumor efficacy of the dual radiosensitive platform and induced the synergistically therapeutic efficiency against tumor.

To further demonstrate the generic nature of the developed therapeutic modality against different tumor types, the therapeutic evaluation was also carried out on the 4T1-tumor xenograft-bearing Balb/c mice model (Fig. 6a). Adopting the same routing, we set different treatments, including group 1: PBS; group 2: RT; group 3: RT + Cyan (with laser irradiation); group 4: RT + BNs; group 5: RT + BNs + Cyan (with laser irradiation). The tumors sites in the combined treatment group were subjected a 6 Gy dose of X-ray 30 min after administration of cyanobacteria followed by laser irradiation (660 nm, 50 mW cm^{-2}, 10 min). During the monitoring interval, the tumor size and body weight were recorded every other day. At the end of follow-up, mice were euthanized and carried out *ex vivo* assessment (Fig. 6b–e). It was obvious that RT + BNs + Cyan group exhibited the most valid suppression on tumor growth and no apparent side effect was observed. Tumor tissues from each group were harvested and photographed (Fig. 6f). Consistent with the LLC-tumor xenograft-bearing C57/B6 mice model, RT + BNs + Cyan group achieved the best inhibition rate (81.3%) as compared to RT (23.9%), RT + Cyan (with 660 nm irradiation) (28.6%) and RT + BNs (59.9%). According to the results of H&E staining, Ki-67 immunohistochemistry staining and the apoptosis indicator TUNEL staining in the tumor sections (Fig. 6g, Fig. S16b), the maximal level of apoptosis and the lowest proliferation proportion were observed in the RT + BNs + Cyan group. From the pathological features of the dissected major organs, eligible *in vivo* treatment biosafety of cyanobacteria and BNs were also demonstrated (Fig. S15). All these results demonstrated the outstanding profile on RT-enhanced outcome against tumor. The evaluations on different tumor models further verify this dual-sensitized RT modality based on TME-mediating photosynthetic oxygenation by cyanobacteria and radio-sensitizing effect of 2D bismuthene.

4. Conclusions

In summary, we have engineered a biomimetic *in-situ* oxygen-evolving platform by the rational combination of natural photosynthetic cyanobacteria with the distinct 2D bismuthene nanosheet, a superior X-ray energy absorption agent, for double-enhanced tumor radiosensitization, which simultaneously achieved the modulation of hypoxic condition in TME and overproduced considerable ROS subsequently. Under light activation, the functional cyanobacteria component induced the tumor oxygenation by the specific photosynthesis for alleviating tumor hypoxia. Especially, the integrated 2D bismuthene nanosheets acted as the radio-sensitizing nanoagents for further enhancing the radiotherapeutic efficacy. The high therapeutic efficacy and desirable therapeutic outcome were systematically demonstrated on two different tumor-bearing animal models, *i.e.*, LLC-tumor xenograft and 4T1-tumor xenograft mice model, in accompany with the demonstrated high biocompatibility and therapeutic biosafety both *in vitro* and *in vivo*. This work provides the representative paradigm of augmenting the therapeutic efficacy of tumor radiotherapy by dual strategies, *i.e.*, hypoxia alleviation by cyanobacteria-enabled photosynthetic oxygenation and ROS overproduction by 2D bismuthene as radio-sensitizing agent, which not only introduces the microbial therapy into tumor radiotherapy but also expands the biomedical utilization of 2D bismuthene.

CRediT authorship contribution statement

Rong Chai: Conceptualization, Methodology, Investigation, Writing – original draft. **Luodan Yu:** Investigation, Writing – review & editing. **Caihong Dong:** Investigation, Visualization. **Yipengchen Yin:** Visualization. **Sheng Wang:** Investigation. **Yu Chen:** Conceptualization, Supervision, Writing – review & editing, Funding acquisition. **Qin Zhang:** Supervision, Writing – review & editing, Funding acquisition.

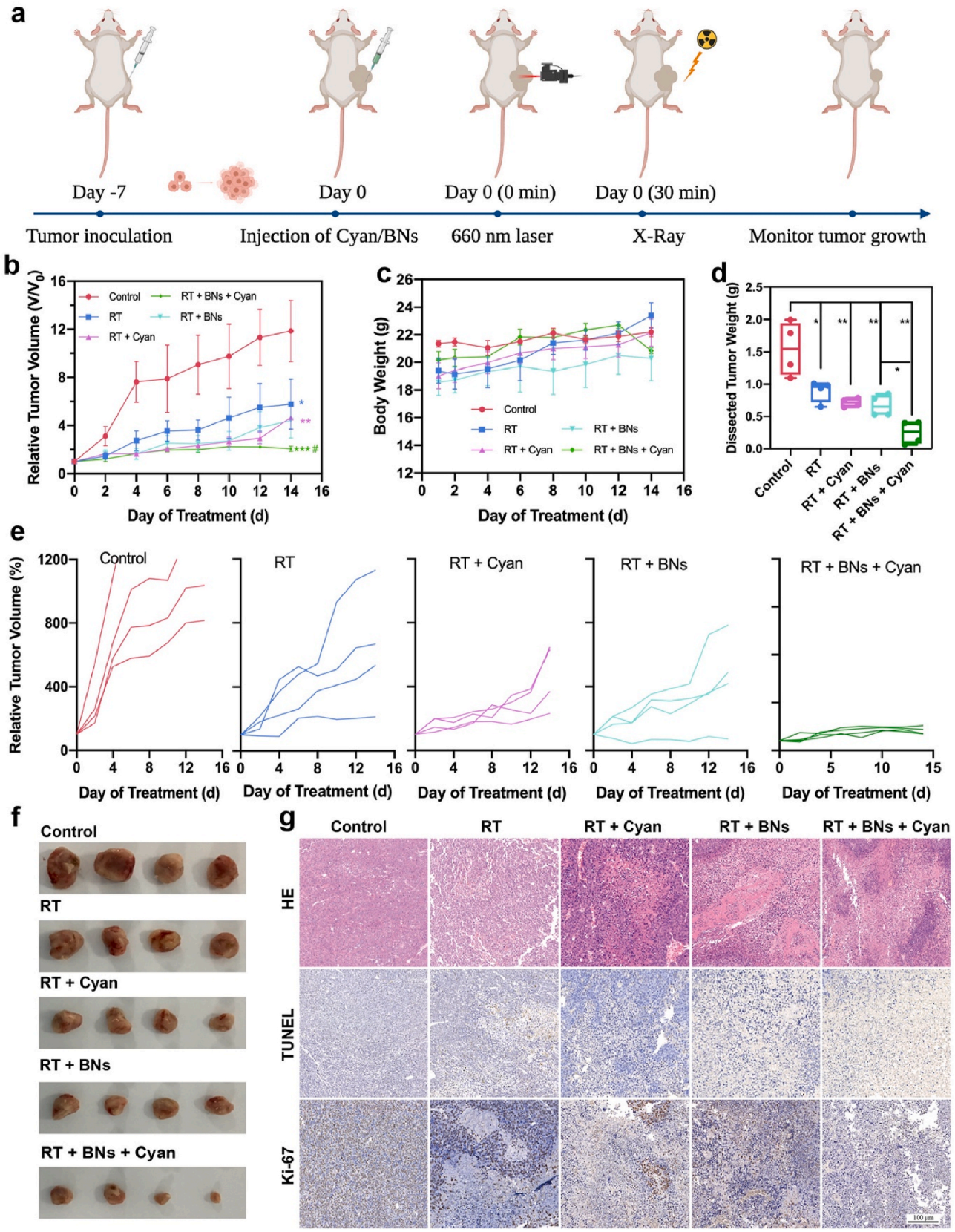

Fig. 6. *In vivo* tumor radiotherapy on the 4T1-tumor xenograft-bearing Balb/c mice model. (a) Schematic illustration of Cyan/BNs-enhanced tumor radiotherapy *in vivo* (Created with BioRender.com). **(b)** Tumor volumes and **(c)** body weights for each group of mice recorded every 2 days after various treatments (n = 4). **(d)** Average tumor weights for each group of dissected xenografts recorded after various treatments. **(e)** Individual tumor-growth curves of mice after various treatments: group 1 for PBS, group 2 for RT, group 3 for RT + Cyan (with 660 nm laser irradiation), group 4 for RT + BNs and group 5 for RT + BNs + Cyan (with 660 nm laser irradiation). **(f)** Digital photos of dissected tumors after various treatments. **(g)** H&E, TUNEL, and antigen Ki-67 analysis of tumor slices subjected to various treatments. All data are presented as mean ± SD. *P < 0.05, **P < 0.01 compared to the control group. $^{###}$P < 0.001 compared to the RT group.

Declaration of competing interest

The authors declare no competing financial interest.

Acknowledgements

R.C. and L.Y. contributed equally to this work. The authors greatly acknowledge the financial support from the National Natural Science Foundation of China (Grant Nos. 81703021, 81772604), Basic Research Program of Shanghai Municipal Government (Grant No. 21JC1406002), Shanghai Science and Technology Program (Grant No. 21010500100), Youth Program of National Natural Science Foundation of China (Grant No. 51902334) and Shanghai Pujiang Program (2020PJD56). The authors greatly thank Dr. Mei Gao at Shanghai Jiao Tong University (SJTU) for her technical supports on the PA imaging.

Appendix A. Supplementary data

Supplementary data to this article can be found online at https://doi.org/10.1016/j.bioactmat.2022.01.014.

References

[1] D. Schaue, W.H. McBride, Nat. Rev. Clin. Oncol. 12 (9) (2015) 527–540.
[2] X. Chen, J. Song, X. Chen, H. Yang, Chem. Soc. Rev. 48 (11) (2019) 3073–3101.
[3] Y. Duo, Y. Huang, W. Liang, R. Yuan, Y. Li, T. Chen, H. Zhang, Adv. Funct. Mater. 30 (4) (2020), 1906010.
[4] M. Baumann, M. Krause, J. Overgaard, J. Debus, S.M. Bentzen, J. Daartz, C. Richter, D. Zips, T. Bortfeld, Nat. Rev. Cancer 16 (4) (2016) 234–249.
[5] G.L. Semenza, N. Engl. J. Med. 365 (6) (2011) 537–547.
[6] D. Kwatra, A. Venugopal, S. Anant, Transl. Cancer Res. 2 (4) (2013) 330–342.
[7] G.L. Semenza, Annu. Rev. Pathol. 9 (2014) 47–71.
[8] D. De Ruysscher, G. Niedermann, N.G. Burnet, S. Siva, A.W.M. Lee, F. Hegi-Johnson, Nat. Rev. Dis. Prim. 5 (1) (2019) 13.
[9] G. Song, Y. Chen, C. Liang, X. Yi, J. Liu, X. Sun, S. Shen, K. Yang, Z. Liu, Adv. Mater. 28 (33) (2016) 7143–7148.
[10] Q. Chen, L. Feng, J. Liu, W. Zhu, Z. Dong, Y. Wu, Z. Liu, Adv. Mater. 28 (33) (2016) 7129–7136.
[11] C.P. Liu, T.H. Wu, C.Y. Liu, K.C. Chen, Y.X. Chen, G.S. Chen, S.Y. Lin, Small 13 (26) (2017), 1700278.
[12] Q. Xiao, X. Zheng, W. Bu, W. Ge, S. Zhang, F. Chen, H. Xing, Q. Ren, W. Fan, K. Zhao, Y. Hua, J. Shi, J. Am. Chem. Soc. 135 (35) (2013) 13041–13048.
[13] M. Huo, L. Wang, L. Zhang, C. Wei, Y. Chen, J. Shi, Angew. Chem. Int. Ed. 59 (5) (2020) 1906–1913.
[14] S. Wang, Y. Duan, Q. Zhang, A. Komarla, H. Gong, W. Gao, L. Zhang, Small Struct. 1 (1) (2020), 2000018.
[15] Y. Qiao, F. Yang, T. Xie, Z. Du, D. Zhong, Y. Qi, Y. Li, W. Li, Z. Lu, J. Rao, Y. Sun, M. Zhou, Sci. Adv. 6 (21) (2020), eaba5996.
[16] M. Huo, P. Liu, L. Zhang, C. Wei, L. Wang, Y. Chen, J. Shi, Adv. Funct. Mater. 31 (16) (2021), 2010196.
[17] G. Luan, X. Lu, Biotechnol. Adv. 36 (2) (2018) 430–442.
[18] X. Kong, X. Chong, K. Squire, A.X. Wang, Sensor. Actuator. B Chem. 259 (2018) 587–595.
[19] S. Managò, G. Zito, A. Rogato, M. Casalino, E. Esposito, A.C. De Luca, E. De Tommasi, ACS Appl. Mater. Interfaces 10 (15) (2018) 12406–12416.
[20] M.N. Chávez, T.L. Schenck, U. Hopfner, C. Centeno-Cerdas, I. Somlai-Schweiger, C. Schwarz, H.G. Machens, M. Heikenwalder, M.R. Bono, M.L. Allende, J. Nickelsen, J.T. Egaña, Biomaterials 75 (2016) 25–36.
[21] H. Chen, Y. Cheng, J. Tian, P. Yang, X. Zhang, Y. Chen, Y. Hu, J. Wu, Sci. Adv. 6 (20) (2020), eaba4311.
[22] D. Zhong, D. Zhang, T. Xie, M. Zhou, Small 16 (20) (2020), e2000819.
[23] T.J. Zhou, L. Xing, Y.T. Fan, P.F. Cui, H.L. Jiang, J. Contr. Release 307 (2019) 44–54.
[24] T. Sun, Y. Zhang, C. Zhang, H. Wang, H. Pan, J. Liu, Z. Li, L. Chen, J. Chang, W. Zhang, Front. Bioeng. Biotechnol. 8 (2020) 237.
[25] J.W. Schopf, The fossil record of cyanobacteria, in: B. Whitton (Ed.), Ecology of Cyanobacteria II, Springer, Dordrecht, 2012, pp. 15–36.
[26] M.H. Yao, M. Ma, Y. Chen, X.Q. Jia, G. Xu, H.X. Xu, H.R. Chen, R. Wu, Biomaterials 35 (28) (2014) 8197–8205.
[27] K. Ni, G. Lan, C. Chan, X. Duan, N. Guo, S.S. Veroneau, R.R. Weichselbaum, W. Lin, Matter 1 (5) (2019) 1331–1353.
[28] W. Fan, B. Yung, P. Huang, X. Chen, Chem. Rev. 117 (22) (2017) 13566–13638.
[29] E.C. Pratt, T.M. Shaffer, Q. Zhang, C.M. Drain, J. Grimm, Nat. Nanotechnol. 13 (5) (2018) 418–426.
[30] G. Song, C. Liang, X. Yi, Q. Zhao, L. Cheng, K. Yang, Z. Liu, Adv. Mater. 28 (14) (2016) 2716–2723.
[31] H. Wang, B. Lv, Z. Tang, M. Zhang, W. Ge, Y. Liu, X. He, K. Zhao, X. Zheng, M. He, W. Bu, Nano Lett. 18 (9) (2018) 5768–5774.
[32] J. Xie, L. Gong, S. Zhu, Y. Yong, Z. Gu, Y. Zhao, Adv. Mater. 31 (3) (2019), e1802244.
[33] C. Liu, J. Shin, S. Son, Y. Choe, N. Farokhzad, Z. Tang, Y. Xiao, N. Kong, T. Xie, J. S. Kim, W. Tao, Chem. Soc. Rev. 50 (4) (2021) 2260–2279.
[34] X. Ji, L. Ge, C. Liu, Z. Tang, Y. Xiao, W. Chen, Z. Lei, W. Gao, S. Blake, D. De, B. Shi, X. Zeng, N. Kong, X. Zhang, W. Tao, Nat. Commun. 12 (1) (2021) 1124.
[35] C. Liu, S. Sun, Q. Feng, G. Wu, Y. Wu, N. Kong, Z. Yu, J. Yao, X. Zhang, W. Chen, Z. Tang, Y. Xiao, X. Huang, A. Lv, C. Yao, H. Cheng, A. Wu, T. Xie, W. Tao, Adv. Mater. 33 (37) (2021), e2102054.
[36] W. Tao, N. Kong, X. Ji, Y. Zhang, A. Sharma, J. Ouyang, B. Qi, J. Wang, N. Xie, C. Kang, H. Zhang, O.C. Farokhzad, J.S. Kim, Chem. Soc. Rev. 48 (11) (2019) 2891–2912.
[37] Y. Wang, W. Feng, M. Chang, J. Yang, Y. Guo, L. Ding, L. Yu, H. Huang, Y. Chen, J. Shi, Adv. Funct. Mater. 31 (6) (2021), 2005093.
[38] Z. Yang, J. Wen, Q. Wang, Y. Li, Y. Zhao, Y. Tian, X. Wang, X. Cao, Y. Zhang, G. Lu, Z. Teng, L. Zhang, ACS Appl. Mater. Interfaces 11 (1) (2019) 187–194.
[39] D.C. Singleton, A. Macann, W.R. Wilson, Nat. Rev. Clin. Oncol. 18 (12) (2021) 751–772.
[40] Y. Zang, L. Gong, L. Mei, Z. Gu, Q. Wang, ACS Appl. Mater. Interfaces 11 (21) (2019) 18942–18952.
[41] H. Sung, J. Ferlay, R.L. Siegel, M. Laversanne, I. Soerjomataram, A. Jemal, F. Bray, CA A Cancer J. Clin. 71 (3) (2021) 209–249.
[42] A. Ullah, S.W. Leong, J. Wang, Q. Wu, M.A. Ghauri, A. Sarwar, Q. Su, Y. Zhang, Cell Death Dis. 12 (5) (2021) 490.